*Andean Geology 52 (2): 221-238. May, 2025*
doi: 10.5027/andgeoV52n2-3762

***Andean Geology***
*www.andeangeology.cl*

# Microscopic analysis of garnet morphology in Santander Massif sillimanite-cordierite hornfels: Constraints on crystal nucleation and growth

**Carlos Alberto Chacón-Ávila[1], Carolina Luna-Mendoza[1], *Carlos Alberto Ríos-Reyes[2], Óscar Mauricio Castellanos-Alarcón[3], Hugo Armando Estupiñán-Durán[4], Carlos Augusto Zuluaga-Castrillón[5], Carolina Jiménez-Triana[5]**

[1] *Escuela de Física, Universidad Industrial de Santander, Cra 27 Cl 9, Bucaramanga, Colombia. carlosalbertoch@gmail.com, caroluna8007@gmail.com*

[2] *Escuela de Geología, Universidad Industrial de Santander, Cra 27 Cl 9, Bucaramanga, Colombia. carios@uis.edu.co*

[3] *Departamento de Geología, Universidad de Pamplona, Autopista Internacional Vía Los Álamos-Villa Antigua, Villa del Rosario, Colombia. oscarmca@yahoo.es*

[4] *Facultad de Minas, Universidad Nacional de Colombia, Cra 65 No. 59A-110, Medellín, Colombia. haestupinand@unal.edu.co*

[5] *Departamento de Geociencias, Universidad Nacional de Colombia, Cra 45 No. 26-85, Bogotá, Colombia. cazuluagacas@unal.edu.co, cjimenez@gmail.com*

[*] *Corresponding author: carios@uis.edu.co*

**ABSTRACT.** Understanding crystal growth in high-grade metamorphic rocks provides unique insights into metamorphic processes and geological evolution. This study investigates the petrographic characteristics, crystal growth mechanisms, and chemical composition of garnets from the Santander Massif of Colombia, a region known for its high-grade metamorphic rocks. Petrographic analysis reveals a discrepancy between anhedral to subhedral garnet forms on an outcrop scale and euhedral forms in hand samples, which may be due to limited or heterogeneous pressure and temperature conditions or spatial constraints at the outcrop scale, and more homogeneous conditions at the hand sample scale. Advanced techniques, including scanning electron microscopy (SEM) and atomic force microscopy (AFM), show that garnet crystals predominantly exhibit trapezohedral {211} and dodecahedral {110} faces, indicating different growth mechanisms. Electron probe microanalysis (EPMA) reveals a homogeneous chemical composition in the garnets, predominantly almandine with minor pyrope, grossular, and spessartine components. The application of cathodoluminescence (CL) and differential interference contrast (DIC) microscopy provides additional insights into mineral characteristics and growth features, contributing to a comprehensive understanding of garnet formation. These findings offer new valuable perspectives on the metamorphic conditions and processes of the rocks that form the Santander Massif.

*Keywords: Microscopy techniques, Santander Massif, Crystal morphology, Garnet, Nucleation and growth.*

**RESUMEN. Análisis microscópico y morfológico de granates en el hornfels sillimanita-cordierita del Macizo de Santander: condiciones de nucleación y crecimiento.** La comprensión del crecimiento cristalino en rocas metamórficas de alto grado ofrece una visión única sobre sus procesos metamórficos y evolución geológica. Este estudio examina las características petrográficas, los mecanismos de crecimiento cristalino y la composición química de los granates provenientes del Macizo de Santander, Colombia, una región destacada por sus rocas metamórficas de alto grado. El análisis petrográfico de los granates reporta una discrepancia entre las formas anhedrales a subhedrales a escala del afloramiento y las formas euhedrales a escala de la muestra de mano. Esto puede deberse a condiciones limitadas o heterogéneas de presión y temperatura o restricciones espaciales a escala del afloramiento y condiciones más homogéneas a escala de la muestra de mano. Técnicas analíticas avanzadas, como la microscopía electrónica de barrido (SEM) y la microscopía de fuerza atómica (AFM), revelan que los cristales de granate presentan predominantemente formas trapezoédricas {211} y dodecaédricas {110}, lo que indica diferentes mecanismos de crecimiento. El análisis mediante microsonda electrónica (EPMA) muestra una composición química homogénea en los granates, rica en almandino, con componentes menores de piropo, grosularia y espesartina. El uso de técnicas como la catodoluminescencia (CL) y la microscopía de contraste de interferencia diferencial (DIC) proporciona una visión más detallada sobre las características y el crecimiento de estos minerales, lo que contribuye a una comprensión más completa sobre su formación. Estos hallazgos ofrecen una nueva perspectiva sobre los procesos y las condiciones metamórficas de las rocas que conforman el Macizo de Santander.

*Palabras clave: Técnicas de microscopía, Macizo de Santander, Morfología cristalina, Granate, Nucleación y crecimiento.*

## 1. Introduction

Garnet, a mineral with the general formula $A_3B_2M_3O_{12}$, where A=(Mg, Mn, Ca, Fe)$^{2+}$; B=(Al, Cr, Ti, Zr, Mn, V, Fe)$^{3+}$; and M=Si, which can be partially substituted by Fe and Al (Mandarino and Back, 2004), is a key component in the study of metamorphic rocks due to its ability to preserve a detailed record of its formation. The formation of garnet is one of the most common reactions in the crust (*e.g.*, Ague and Carlson, 2013), being therefore one of the most studied minerals in relation with chemical variations in metamorphic rocks (*e.g.*, Jamtveit *et al*., 1993; Jamtveit and Hervig, 1994; Spear and Kohn, 1996; Baxter and Scherer, 2013; Dragovic *et al*., 2018). In fact, garnet preserves a good record of its growth history, expressed by its chemical zoning and mineral inclusions, and by its broad compositional range, which promotes the growth of garnet in metamorphic rocks over a wide spectrum of chemical compositions and metamorphic conditions (*e.g.*, Carlson *et al*., 1995; Ríos *et al*., 2008; Kretz, 2010; Ague and Carlson, 2013; Gulbin and Glazov, 2013; Inui *et al*., 2020; Zhu *et al*., 2022; Kohn *et al*., 2024; Li *et al*., 2024). In addition, its refractory character allows the preservation of chemical and textural zoning that is important when making interpretations about the metamorphic history of the host rock.

A garnet crystal forms during extended geochemical reactions, with its growth tightly controlled by pressure, temperature, and other thermodynamic parameters (*e.g.*, Inui *et al*., 2020). These parameters influence the mineral's crystallization processes by determining the stability and availability of the necessary chemical components. Understanding how garnets form represents a crucial challenge since at least the 1970s, with diffusion-controlled processes widely applied to study garnet-forming reactions (Carlson, 1989; Miyazaki, 1991, 1996; Carlson *et al*., 1995); nevertheless, a thorough understanding of these forming processes at the atomic scale is still a subject relatively unexplored.

Differential Interference Contrast (DIC) microscopy is a powerful optical technique that introduces contrast in transparent samples. Cathodoluminescence (CL) is a useful tool for studying the garnet's internal structure and for providing a rapid identification of other mineral phases (*e.g.*, Imashuku and Wagatsuma, 2020). Scanning Electron Microscopy (SEM) and Atomic Force Microscopy (AFM) are two of the most powerful microscopy techniques available today for the investigation of the surface structure of minerals with resolution at the nanometer of even atomic level. AFM, in particular, has been used to study the morphology and the charge characteristics of mineral and oxide particles (*e.g.*, Anderson *et al*., 2007; Drelich and Wang, 2011; Wenderich *et al*., 2014), to characterize clay particles (*e.g.*, Gupta and Miller, 2010; Kumar *et al*., 2016), and to observe mineral dissolution (*e.g.*, Maurice *et al*., 1995; Dove and Platt, 1996; Klasa *et al*., 2013), nucleation (Dove and Hochella, 1993), growth (*e.g.*, Georgiev *et al*., 2013; Renard *et al*., 2013; Bracco *et al*., 2016), and

epitaxial metal precipitation (Junta and Hochella, 1994). Electron Probe Microanalysis (EPMA) is an analytical technique used to determine the elemental composition of minerals and other materials with high spatial resolution, providing detailed information about the chemical composition and zoning patterns within minerals, which is crucial for understanding their formation and metamorphic histories.

Although scientific investigations that use both SEM and AFM techniques are common, there are just a few works that directly discuss their complementary nature (*e.g.*, Campbell *et al*., 1999; Reynolds and Taylor, 1999; Russell *et al*., 2001). This study therefore presents the combined use of SEM and AFM images to examine the nucleation and growth of garnet at nanoscopic scales from a sillimanite-cordierite hornfels in the Santander Massif of Colombia. In the next section, we provide a brief overview of the metamorphic evolution and the specific heat-driven processes that influenced the geological unit from which the garnet-bearing hornfels were sourced: the Bucaramanga Gneiss Formation.

## 2. Geological background

The Santander Massif (SM), located in the northeastern part of Colombia, is a major component of the Northern Andean orogenic basement (*e.g.*, Gansser, 1973; Aleman and Ramos, 2000; Restrepo-Pace and Cediel, 2010; van der Lelij *et al*., 2016). The SM is composed of pre-Devonian metamorphic rocks intruded by bodies of Triassic to Cretaceous ages (*e.g.*, Goldsmith, 1971; Ward *et al*., 1973; Boinet *et al*., 1985; Royero and Clavijo, 2001; Bustamante *et al*., 2016). The metamorphic basement of the SM is divided into three main units: the Bucaramanga Gneiss Formation (BGF), the Silgará Formation (SF), and the Orthogneiss (O) (*e.g.*, Ward *et al*., 1973; Ríos *et al*., 2003; García *et al*., 2005; Rey and García, 2015). These units are overlain by the unmetamorphosed Floresta Formation, which is unconformably overlain by Carboniferous and Permian clastic to calcareous rocks. Triassic sedimentary rocks of the Tiburón Formation lie above these sequences. Another post-Paleozoic units include the Bocas and Jordán formations; the latter consists of fine-grained red beds with interlayered volcanic rocks and intrusive clasts and is discordantly overlain by the red bed sequence of the Jurassic Girón Formation. Cretaceous sedimentary rocks are found around the SM, preserved as erosional remnants. The geographical location of the SM in the Colombian Andes and a generalized geological map of the study area are presented in figure 1.

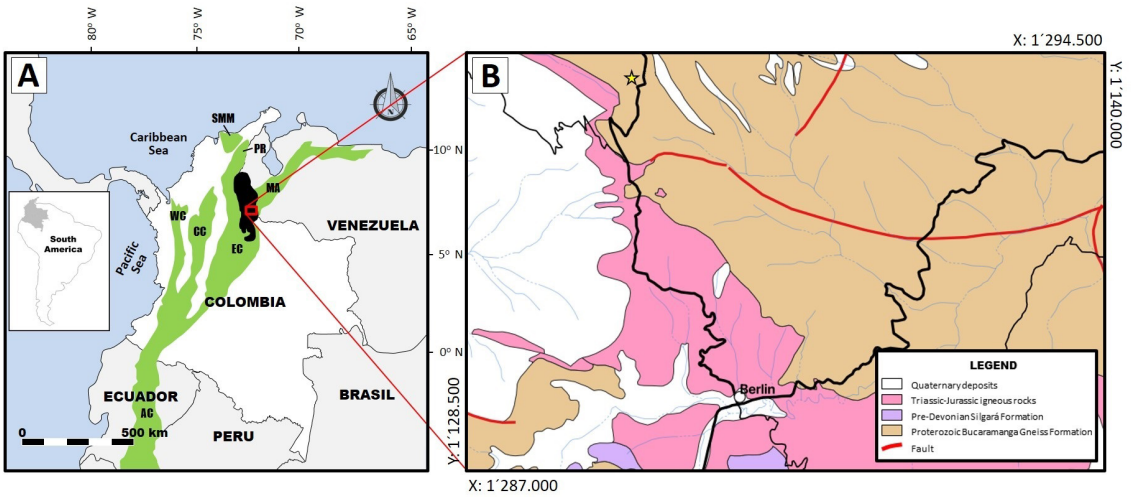


FIG. 1. **A.** Geographical location of the Santander Massif (in black color) in the Colombian Andes and location of the study area (red rectangle). **B.** Generalized geological map of the study area. Yellow star indicates sample locality. **AC**: Andes Cordillera, **CC**: Central Cordillera, **EC**: Eastern Cordillera, **MA**: Mérida Andes, **PR**: Perijá Range, **SMM**: Santa Marta Massif, and **WC**: Western Cordillera.

The BGF is a key component of the igneous-metamorphic basement of the SM since it represents the oldest (Precambrian) geological unit in the region. It is characterized by a succession of pelitic and semipelitic gneisses intercalated with thin layers of calc-silicate rocks, marbles, hornblende gneisses, and amphibolites. In the study area, this formation primarily consists of quartz-feldspar biotite and sillimanite gneisses, along with hornblende gneisses, quartzites, and amphibolites. These rocks underwent high-temperature (HT) contact metamorphism, reaching the amphibolite facies. This HT event, driven by the intrusion of magmatic bodies or elevated geothermal gradients, significantly influenced the mineralogical composition and textural characteristics of the rocks, including the formation of hornfels. The estimated metamorphic conditions range from 5.0-9.5 kbar and 630-750 °C, indicative of Barrovian-type metamorphism, which is marked by the development of three metamorphic zones: staurolite-kyanite, sillimanite-cordierite, and migmatite (*e.g*., Castellanos, 2001; García *et al*., 2005; Urueña and Zuluaga, 2011). These estimates were further refined by Jiménez-Triana (2016), reporting 5.3-9.0 kbar and 835-897 °C.

## 3. Materials and methods

In this study, several garnet crystals within a sillimanite-cordierite hornfels sample were analyzed. Specifically, a single garnet crystal was selected for detailed analysis using SEM and AFM, due to its specific characteristics that allowed high-resolution inspection of its morphology and surface structure. On the other hand, multiple garnet crystals from the same rock were analyzed using DIC, CL, and EPMA techniques, in order to obtain a broader view of the compositional and structural variability of the crystals within the sample. The garnet-bearing sillimanite-cordierite hornfels was collected along the road from Berlin to Vetas in the Department of Santander (Fig. 1B). The rock sample was meticulously hand-picked from the outcrop to ensure it contained enough garnet crystals of interest. Additionally, care was taken to select samples with visible garnet crystals and minimal weathering or alteration. A polished thin section was prepared for transmitted light microscopy (Olympus BX50) and CL measurements. The CL analysis was performed on a CL8200 Mk5-2 (Cambridge Image Technology Ltd.) optical CL stage attached to a Leica DM2500 P petrographic microscope under the following operating conditions: 20 kV (accelerating voltage), 300 μA (beam current), and 0.003 mBar (window vacuum pressure). Images were captured using a Leica DFC450 camera. Mineral abbreviations and symbols were adopted according to the standards established by Warr (2021).

DIC images were obtained using a Zeiss Axio Imager Z1 motorized microscope with high-resolution capabilities (200 nm in X-Y and 10 nm in Z). The microscope was equipped with an AxioCam HRc camera, which allowed for the rapid acquisition of color images with a pseudo-relief effect, thus providing detailed three-dimensional contrast. SEM images were obtained using a FEI Quanta 650 FEG SEM microscope to observe the crystal size and shape. To enhance conductivity, the garnet was previously mounted on a metal stub using carbon tape and then sputter-coated with a thin layer of carbon to enhance conductivity. The SEM analysis was conducted under the following analytical conditions: 120-4000x (magnification), 8.5-10.0 mm (working distance), 30 kV (acceleration voltage), ETD (detector), and SE (mode). EPMA analyses were performed using a JEOL JXA-8230 EPMA, under the following analytical conditions: 15 kV (acceleration voltage), 20 nA (beam current, analysis), 300 nA (beam current, mapping), 1 μm (beam size), and 10 s (counting time, peak and background). Data acquisition and reduction were carried out using ZAF (atomic number, absorption, fluorescence) correction procedures. Natural and synthetic minerals were used as standards. Spot analyses were conducted at multiple locations on the crystal. AFM images were acquired using a Park NX10 AFM in contact mode. For surface roughness determination, scans were performed on a sample of 90 $\mu m^2$, while for grain size analysis the scans were conducted on areas of 45 μm x 45 μm. The scan rate was set between 0.4 and 0.5 Hz, with a set point of 56.67 nN. Standard silicon nitride tips with a nominal radius of 10 nm and a spring constant of 0.58 N/m were used to acquire the images of the garnet's surface topography. Image resolution was 10 nm (lateral) and 1 nm (vertical). Detailed examination of textures was performed using DIC microscopy, SEM, and AFM. The DIC images provided insights into three-dimensional surface variations and crystal face morphology. The SEM imaging revealed the garnet's surface topology, including the presence of dodecahedral and trapezohedral faces and detailed striations and terraces. The AFM images provided high-resolution data on surface roughness and grain size, allowing for the analysis of fine textural features

and surface characteristics. Finally, the EPMA provided estimates on the mineral composition of garnets, providing insights into their chemical properties and growth conditions.

## 4. Results

### 4.1. Petrography, catodoluminiscence, and differential interference contrast

The studied rock is characterized by a granoblastic texture with the mineral assemblage quartz+plagio clase+microcline+garnet+sillimanite+cordierite+ chrysoberyl (Fig. 2A, B). The granoblastic domains include quartz, plagioclase with polysynthetic twinning, and incipient alteration to sericite, as well as microcline or orthoclase. Fibrolitic sillimanite aggregates, spatially related to muscovite and garnet, sometimes anastomosing, indicate the development of incipient, discontinuous foliation between quartz-feldspar domains. Garnet porphyroblasts are abundant in these samples. Garnet is inclusion-free, showing an anhedral to subhedral shape and crystal sizes ranging from 150 to 300 µm. Garnet and quartz crystals showed no detectable luminescence in CL images, although this technique was useful to recognize plagioclase (light green), microcline-orthoclase (dark brownish blue), and fibrolitic sillimanite (dark green) (Fig. 2C). On the other hand, the typical dodecahedral and trapezohedral faces of garnet, with rhomb-shaped terraces at one of its vertices, was identified in DIC images (Fig. 2D, E). All the above suggest the analyzed rock belongs to the higher-grade metamorphic (sillimanite) zone proposed in previous studies (*e.g.*, Castellanos, 2001; Castellanos *et al.*, 2004, 2008; Jiménez-Triana, 2016).

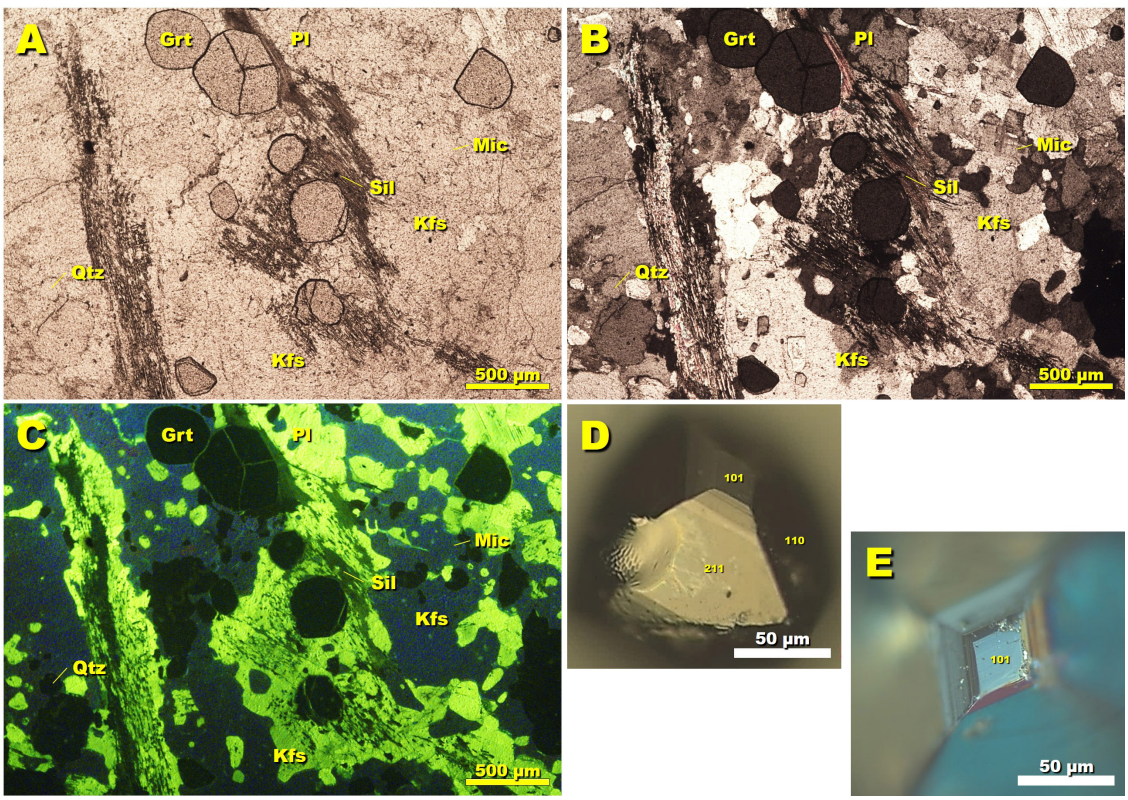


FIG. 2. Photomicrographs of the garnet-bearing sillimanite-cordierite hornfels in plane (**A**) and cross (**B**) polarized light. (**C**) CL image of the garnet-bearing hornfels, showing the brightness contrast between the garnet and the matrix, fractures or edges on the garnet, mineral inclusions, and the relationship between the garnet and surrounding minerals. (**D**)-(**E**) DIC images of one of the vertices of a garnet specimen, showing a detailed visualization of the crystal's surface topography, particularly of the stacked rhomb-shaped terraces. **Grt**: garnet; **Kfs**: K-feldspar; **Mic**: microcline; **Pl**: plagioclase; **Qtz**: quartz; **Sil**: sillimanite.

### 4.2. Scanning Electron Microscopy

The morphology of the analyzed garnet crystal corresponds to a combination of a trapezohedron and a dodecahedron. It is largely bounded by the rhombic to pseudohexagonal faces of the trapezohedron {211} and the smaller rhombic faces of the dodecahedron {110}. These forms are commonly observed in garnets worldwide and generally occur together more frequently than other forms on a single crystal (*e.g.*, Bennema *et al*., 1983; Boutz and Woensdregt, 1993). According to Kretz (2010), the rate of advancement of dodecahedral faces relative to trapezohedral faces can be inferred from face size. Since {110} faces are smaller than {211} faces, it is suggested that {110} faces are farther from the crystal center than {211} faces. If the crystal shape was maintained during growth, {110} faces must have advanced more rapidly than {211} faces, indicating different growth mechanisms. Figure 3 illustrates an idealized sketch of the probable morphological evolution sequence of the studied garnet, with early crystal morphology dominated by dodecahedral shapes, later evolving to a combination of dodecahedral and trapezohedral forms. Figure 3D shows secondary electron (SE) images of the analyzed garnet, displaying the dodecahedral and trapezohedral faces with a rhombic dodecahedron intersecting two

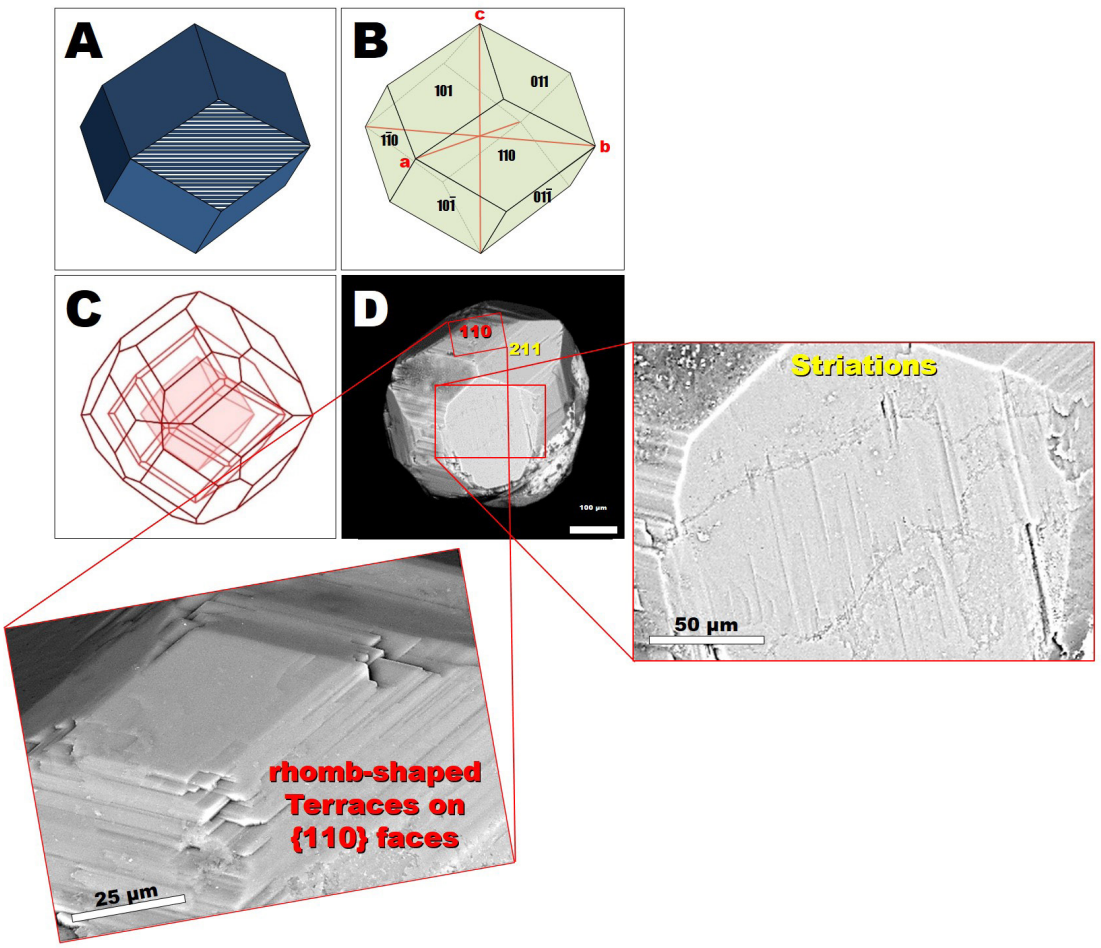


FIG. 3. **A.** Idealized reproduction of a rhombic dodecahedron formed from stacked cubes. **B.** Dodecahedron with its crystal faces. **C.** Morphological evolution sequence of a garnet crystal. **D.** SE images of a well-formed garnet crystal 400 µm in diameter showing its rhombic {110} and rhombic to pseudohexagonal {211} faces (note the striations on {211} and the sharp steps and corners on {110}).

of the crystallographic axes at equal distances and parallel to the z-axis: {110} and a trapezohedron intersecting the z-axis at a unit distance and the other two axes at equal distances: {hhl}. These faces display a smooth ridge-and-valley topography in which the rhomb-shaped terraces are stacked to form a corrugated surface with a curved cross-section, indicating a preference for dodecahedral {110} forms (Fig. 3D). Striations on {211} faces are also visible, showing ridges and valleys with crests approximately 15 µm apart (Fig. 3D).

### 4.3. Electron Probe Microanalysis

Figure 4A shows the EPMA chemical mapping of the garnet-bearing sillimanite-cordierite hornfels. Each mineral is represented by a specific color to facilitate the interpretation of its distribution and abundance in the hornfels. Plagioclase (green) and K-feldspar (blue) are the predominant mineral phases in the hornfels. Other secondary minerals are quartz (gray), cordierite (fuchsia), fibrolitic sillimanite and chrysoberyl (red), and garnet (pink; bottom right part of the figure). The garnet crystal analyzed has the following composition: $SiO_2$ (37.73-37.83 wt%), $Al_2O_3$ (20.71-20.92 wt%), FeO (26.63-26.98 wt%), MnO (10.70-10.88 wt%), MgO (1.95-2.02 wt%), CaO (1.34-1.45 wt%), and $Na_2O$ (0.03-0.05 wt%). The garnets are predominantly almandine-rich ($X_{alm}$=0.63), with minor pyrope ($X_{prp}$=0.08), grossular ($X_{grs}$=0.04), and spessartine ($X_{sps}$=0.25). The Fe/(Fe+Mg) ratio ranges from 0.88 to 0.89. The backscattered electron (BSE) images and X-ray color maps (Fig. 4B, C) indicate that the garnets exhibit homogeneous zoning with consistent levels of $X_{alm}$, $X_{prp}$, $X_{grs}$, and $X_{sps}$ across the analyzed profiles.

### 4.4. Atomic Force Microscopy

AFM images reveal that the crystal faces of garnet exhibit a distinctive faceted morphology with well-defined steps and terraces (Fig. 5). In particular, the images of the {110} face show the presence of individual square terraces at the center of the face, which extend towards the edge of the crystal through step advancement (Fig. 5A). AFM images obtained over an area of 45 µm x 45 µm show an average step height of 13.1 nm (Fig. 5D). Higher-resolution AFM images, captured over a 10.93 µm x 10.93 µm area refine this step height range to 12.497-13.757 nm (Fig. 5E).

## 5. Discussions

### 5.1. Crystal symmetry and growth mechanisms

The study of crystal symmetry in aluminosilicates provides valuable insights into the mechanisms driving their growth. Previous works (*e.g.*, Akizuki, 1981, 1989; Jamtveit and Andersen, 1992) examined the role of step growth in shaping crystal symmetry, with a focus on how interactions between alkali, $Al^{3+}$, and $Si^{4+}$ ions contribute to achieving charge balance. Our results show that the garnet studied in

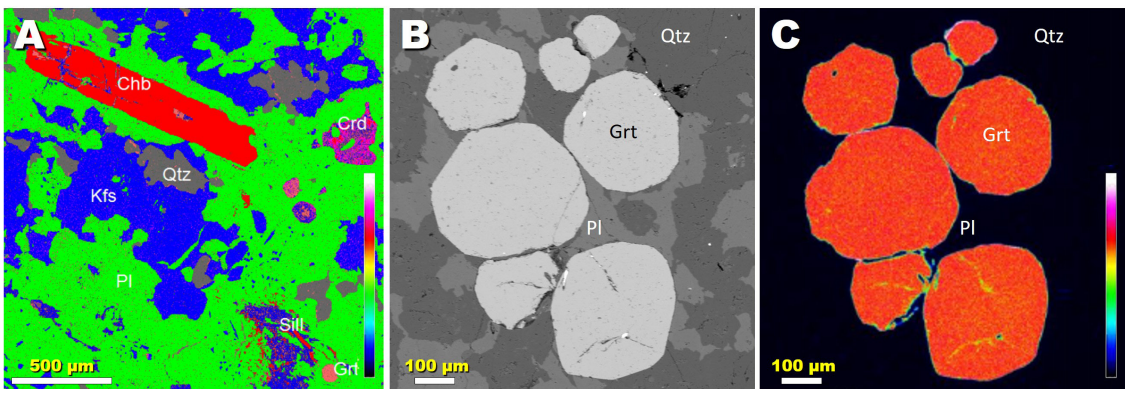


FIG. 4. **A.** EPMA multi-elemental mapping of the garnet-bearing sillimanite-cordierite hornfels. Each mineral has been represented by a specific color to facilitate interpretations. **B.** Back scattered electron (BSE) image. **C.** Mn X-ray color map. In B and C, a homogeneous zoning is evident. **Chb**: chrysoberyl; **Crd**: cordierite; **Grt**: garnet; **Kfs**: K-feldspar; **Pl**: plagioclase; **Qtz**: quartz; **Sill**: fibrolitic sillimanite.

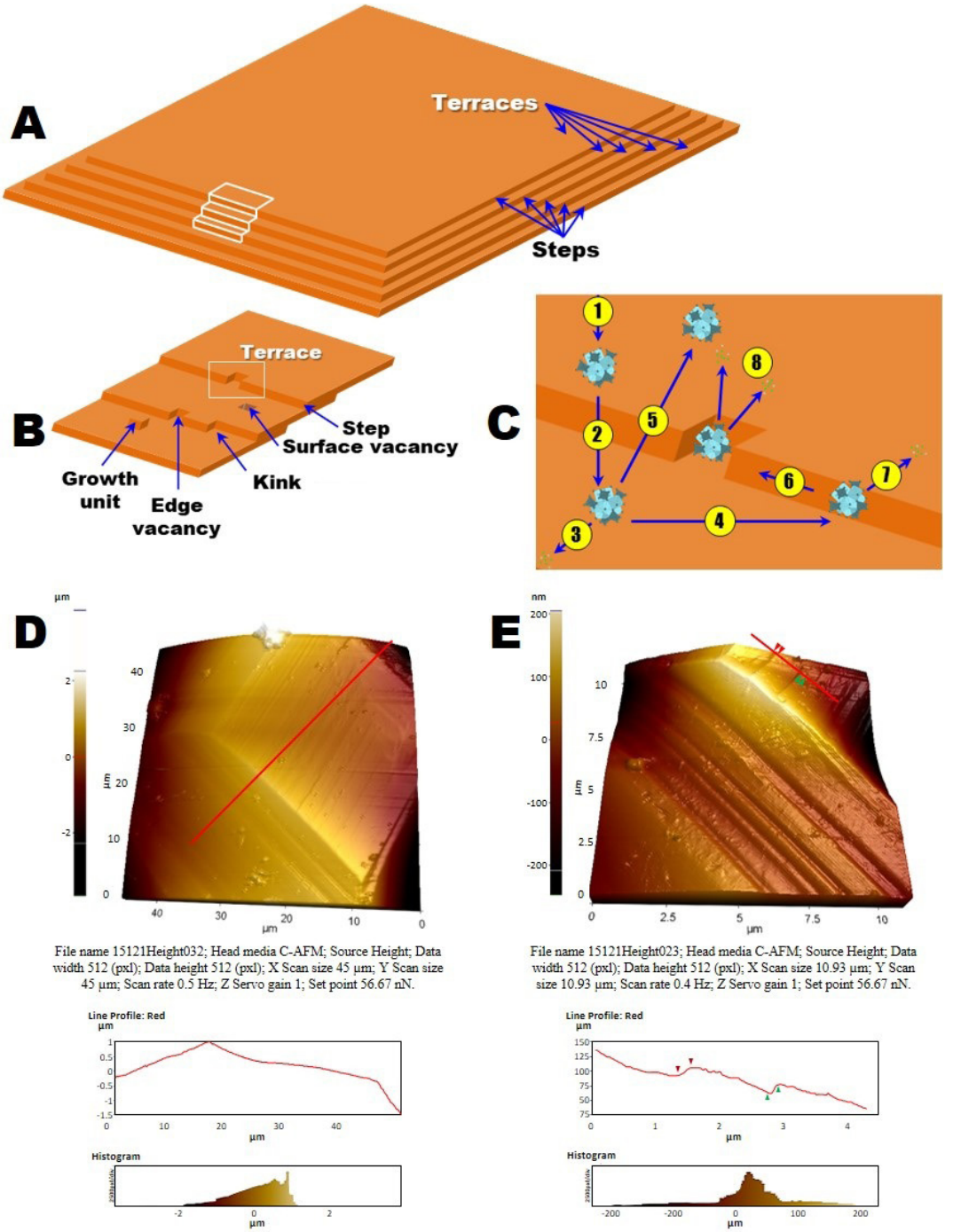


FIG. 5. **A-B.** Kossel model of a crystal surface (modified after Kossel, 1934), showing terraces, steps, and other finer-scale elements. **C.** Schematic representation of the processes involved in crystal growth (modified from Elwell and Scheel, 1975, and Cubillas and Anderson, 2010). Positions 1 to 8 are characterized by different site energies. **D.** 3D AFM image of the garnet surface, scan size 45 µm x 45 µm. **E.** 3D AFM image of one of the garnet vertices, scan size 10.93 µm x 10.93 µm. AFM amplitude signals are shown at the bottom of the figure. Topographic profiles along the red straight lines in the AFM images reveal the step heights and provide additional insights into surface features and crystal growth patterns.

a sillimanite-cordierite hornfels exhibit an anhedral to subhedral morphology at the outcrop scale and euhedral morphology in hand samples, suggesting that formation conditions or dynamics of crystal growth varied across different scales. At the outcrop scale, pressure and temperature may have been heterogeneous and/or spatial conditions more restricted, preventing full development of euhedral forms; hand sample scales, in contrast, may represent more homogeneous areas and more favorable conditions for crystal growth, promoting the formation of euhedral grains. Rapid changes in physiochemical conditions, such as fluid infiltration or rapid heating, may have also played a role in the development of euhedral garnets unless growth occurred during extensive deformation (Rosenfeld, 1970).

### 5.2. Implications for garnet formation

Garnet growth in metamorphic rocks, as observed in the Santander Massif, reflects variations in formation conditions. The occurrence of garnet in a quartz-feldspar hornfels with fibrolitic sillimanite and cordierite, and its association with the sillimanite zone in the Santander Massif, highlights the high-grade metamorphic conditions of the Bucaramanga Formation. These findings corroborate previous studies (Castellanos, 2001; Castellanos *et al*., 2004, 2008; Jiménez-Triana, 2016) that place this formation in a high-grade metamorphic zone. In the present work, we have opted for the use of the term "hornfels", which was probably formed from a quartz-feldspar sandstone, although alternative explanations of its origin need to be considered as well. Regarding the nucleation and growth process of garnet, the combination of dodecahedral and trapezohedral morphologies may stem from the differential growth rates of certain faces. These aspects are explained in more detail below.

### 5.3. Growth mechanisms and morphological features

Previous studies have revealed that garnet crystal growth underscores complex processes (*e.g*., Hergt and Görnert, 1980; Akizuki, 1981, 1989; Jamtveit and Andersen, 1992; Kretz, 2010; Gulbin and Glazov, 2013). Sepahi (2007) suggested that while absolute temperature has minimal impact on garnet crystal morphology, temperature gradients significantly influence crystal shape development, with dodecahedral forms produced under slow temperature gradients and trapezohedral forms under rapid gradients. These growth mechanisms can be further analyzed by focusing on the differences between dodecahedral {110} and trapezohedral {211} faces. In the present study, {110} faces are characterized by stepped rhomb-shaped terraces and they seem to have grown more rapidly than {211} faces, characterized by a smoother ridge-and-valley topography (cf. Kretz, 2010). The observed striations and ridges parallel to the intersection of {211} and {110} faces corroborate previous findings (*e.g*., Akizuki, 1981; Jamtveit and Andersen, 1992; Kretz, 2010). The presence of rhomb-shaped terraces and the corrugated surface on the {110} faces indicate that the growth mechanisms involved a series of nucleation processes. In fact, terraces form and grow around surface vacancies, which are nm-scale regions where atoms are missing (*e.g*., Van *et al*., 2004; Pambudi *et al*., 2021) and create a stepped structure when the terraces are numerous and span the entire length of the crystal (Fig. 5). The irregularity observed in smaller crystals and the random distribution of rhomb-shaped terraces suggest that growth conditions and crystal evolution varied during crystal formation (*e.g*., Acosta-Díaz, 2008). Boutz and Woensdregt's (1993) hypothesis suggests that garnet growth forms are influenced by the effective charges on oxygen, with {211} faces being predominant in fully ionic Si-O bonds. As oxygen effective charges decrease, {110} faces replace {211} faces. In addition to well-formed steps, spiral steps have been reported on {110} and/or {211} faces as well (Endo and Sunagawa, 1968; Jamtveit and Andersen, 1992). Although these spiral steps were not observed in this study, they could be present but undetectable for example due to small step heights.

Computational models (Cherepanova *et al*., 1992a, b) help explain the behavior of interlaced steps and the variation of step velocities in different crystallographic directions on {211} and {110} faces. These models are useful to understand the kinetics of crystal growth and how surface features like steps evolve over time during crystal formation, supporting the hypothesis of layer-by-layer growth and consistent with the observed step and terrace morphology in this study. Knowledge of crystal growth kinetics is important to construct models for

fluid-rock interactions, such as those based on coupled transport and dissolution/precipitation reactions (*e.g*., Steffel and Van Cappelen, 1990). More recently, Tzankova (2007) noted a morphological evolution during garnet growth, with rough growth figures observed on {211} and {110} faces. The striations and growth patterns observed in our sample resemble those described by several authors (*e.g*., Tolksdorf and Welz, 1972; Akizuki, 1981; Jamtveit and Andersen, 1992; Kretz, 2010), where steps, spiral steps, and conical hills were recognized on crystalline surfaces, although in the present study only steps on {110} faces were detected.

To understand the nature of step heights, it is important to determine whether they represent single-layer growth or multiple growth events. Cross-sectional profiles compared with the garnet unit cell dimensions (a=11.531 Å) suggest multiple steps, supporting a layer-by-layer growth mechanism. This is consistent with Kossel's (1934) model, which suggests that crystal surfaces are composed of monatomic-height layers separated by distinct steps, thus explaining the step and terrace morphology. The crystal growth process, as outlined in the literature (*e.g*., Elwell and Scheel, 1975; Cubillas and Anderson, 2010), involves several steps: (1) transport of solute to the crystal surface; (2) diffusion through the boundary layer; (3) adsorption onto the crystal surface; (4) surface diffusion; (5) surface desorption; (6) attachment to a step or edge; (7) diffusion along the step or edge; and (8) incorporation into a kink site or step vacancy, leading to an increase in size (Fig. 5C). 3D AFM images (Fig. 5D, E) provide a detailed perspective of the garnet surface morphology at spatial resolutions of 45 µm x 45 µm and 10.93 µm x 10.93 µm, enhancing our understanding of the growth pattern and the distribution of steps and terraces on the crystal surface, in line with Kossel's theoretical framework.

### 5.4. Chemical diffusion and zoning patterns

The observed homogeneous zoning shown in figure 4B and C suggests that this uniformity is likely due to chemical diffusion occurring during metamorphism. As several authors have noted, diffusion is expected to become more pronounced with increasing metamorphic grade (*e.g*., Anderson and Olimpio, 1977; Ikeda, 1993; Spear, 1993; Yu *et al*., 2019). This process involves the redistribution of chemical components within the garnet as it re-equilibrates with its environment. This chemical homogenization can be attributed to self-diffusion during high- to ultrahigh-temperature metamorphic events (Dharmapriya *et al*., 2017). However, diffusion in garnet reactions occurs slowly over geological timescales (Loomis, 1977), implying that extended periods of high-temperature conditions are needed for significant zoning changes. This suggests that the homogeneous zoning observed reflects a prolonged period of metamorphism during which the garnet had sufficient time to equilibrate and diffuse its components. Possible scenarios for this observed homogenization include post-growth diffusion and the thermal effect of intrusions. One hypothesis is that the original zoning of the garnet was erased due to a cooling phase following the peak of metamorphism, a process discussed by Tracy (1982). Alternatively, another explanation is that the garnet grew near intrusive bodies, such as granitoids. These intrusions could have induced a local thermal effect at relatively shallow depths (<20 km), which may have facilitated the diffusion of the garnet components, resulting in homogeneous zoning (Burenjargal *et al*., 2012). The implication of this finding is that the garnet likely experienced protracted metamorphic conditions that facilitated this chemical homogenization, and supports the idea that the garnet's current homogeneous zoning is indicative of a complex metamorphic history, consistent with previous studies on diffusion in garnets (*e.g*., Kobayashi *et al*., 2011; Massonne and Li, 2020; Li *et al*., 2024; Su *et al*., 2024). The results from this study about homogeneous zoning contrast with the zonation patterns previously reported for the region. For instance, while Castellanos (2001) documents normal, reverse and sectorial zoning, our data show that the garnets display a consistent chemical composition across the analyzed profiles, with uniform levels of $X_{alm}$, $X_{prp}$, $X_{grs}$, and $X_{sps}$. The presence of homogeneous zoning could reflect specific formation or metamorphic conditions that differ from those reported in earlier studies. This finding highlights the need for further investigation into the geological processes that might have influenced this unusual characteristic. Additionally, the absence of typical zonation patterns may have implications for interpreting the geothermal history of the area, as well as for the broader understanding of metamorphic processes in the Santander Massif area.

### 5.5. Nucleation and growth processes

The nucleation and growth of garnets involve several stages (*e.g.*, Meth and Carlson, 2005; Spear, 2017, 2025): dissolution of reactants, transfer of nutrients, growth of inclusion-free garnet, and final homogenization (Figs. 6 and 7). The chemistry of garnet evolution can be influenced by various factors, including the formation of intermediate metastable phases, simultaneous reactions like precipitation and dissolution, and the nucleation and growth of other minerals. The reaction history of the nucleation and growth mechanism of the studied garnet is shown in figure 6 and can be summarized as follows. Interface reactions promoted reactant minerals (Fig. 6A). Aluminosilicates (mainly biotite, quartz, and plagioclase) and oxides (ilmenite) broke down and their chemical constituents went into solution (Fig. 6B), producing the formation of nutrients (ionic species) which were then transported to nucleation sites, indicating that the ionic species were not static. Aluminosilicates mainly provided Si and Al; biotite Fe and Mn (in exchange for Mg to account for the high Fe and Mn concentrations calculated); muscovite alkali elements (Na and K); plagioclase Na and Ca; quartz provided additional Si; and ilmenite Ti. During a metastable state, an aluminosilicate gel (Fig. 6C), probably in equilibrium conditions, provided the precursors for the nucleation of garnet. The gel composition and structure, along with the complexing agents, control the nucleation and growth of garnet crystals. In laboratory settings, these characteristics determine the size and morphology of the crystals, influenced by the type of complexing agents and

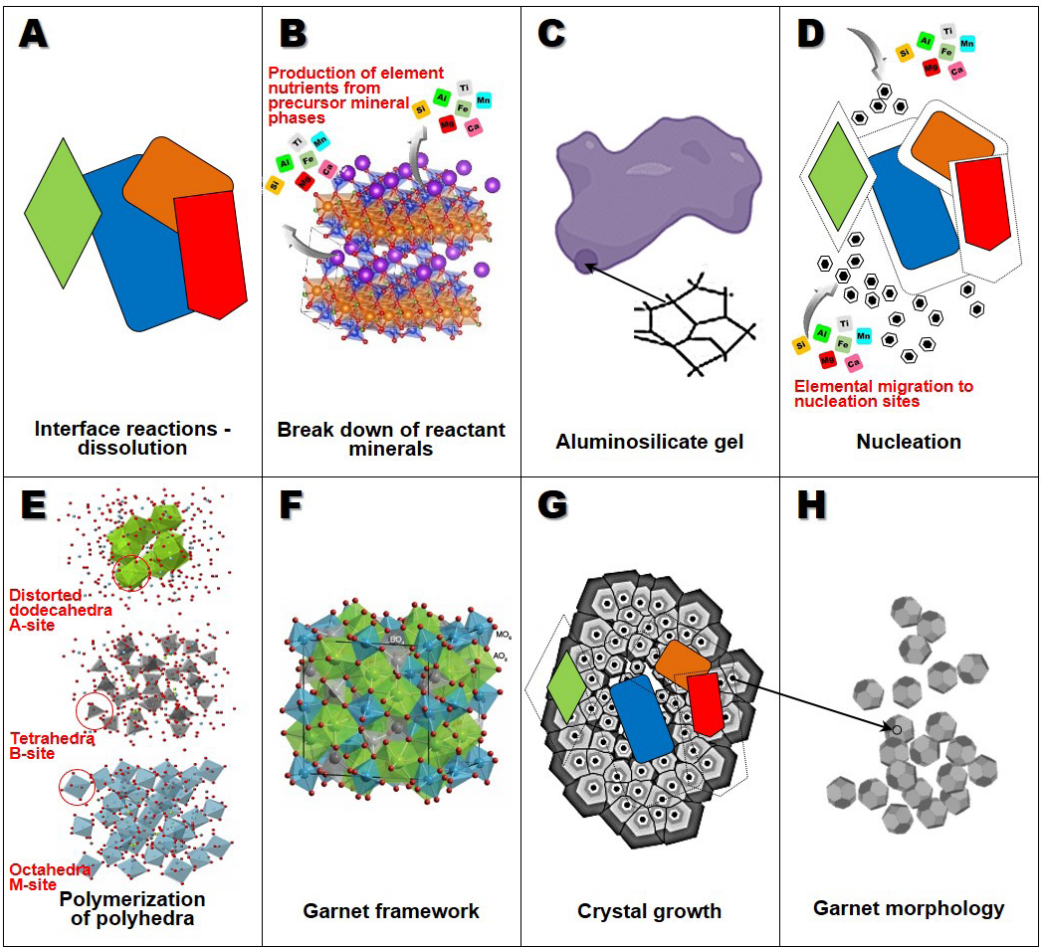


FIG. 6. Reaction history of the nucleation and growth mechanism of the studied garnet.

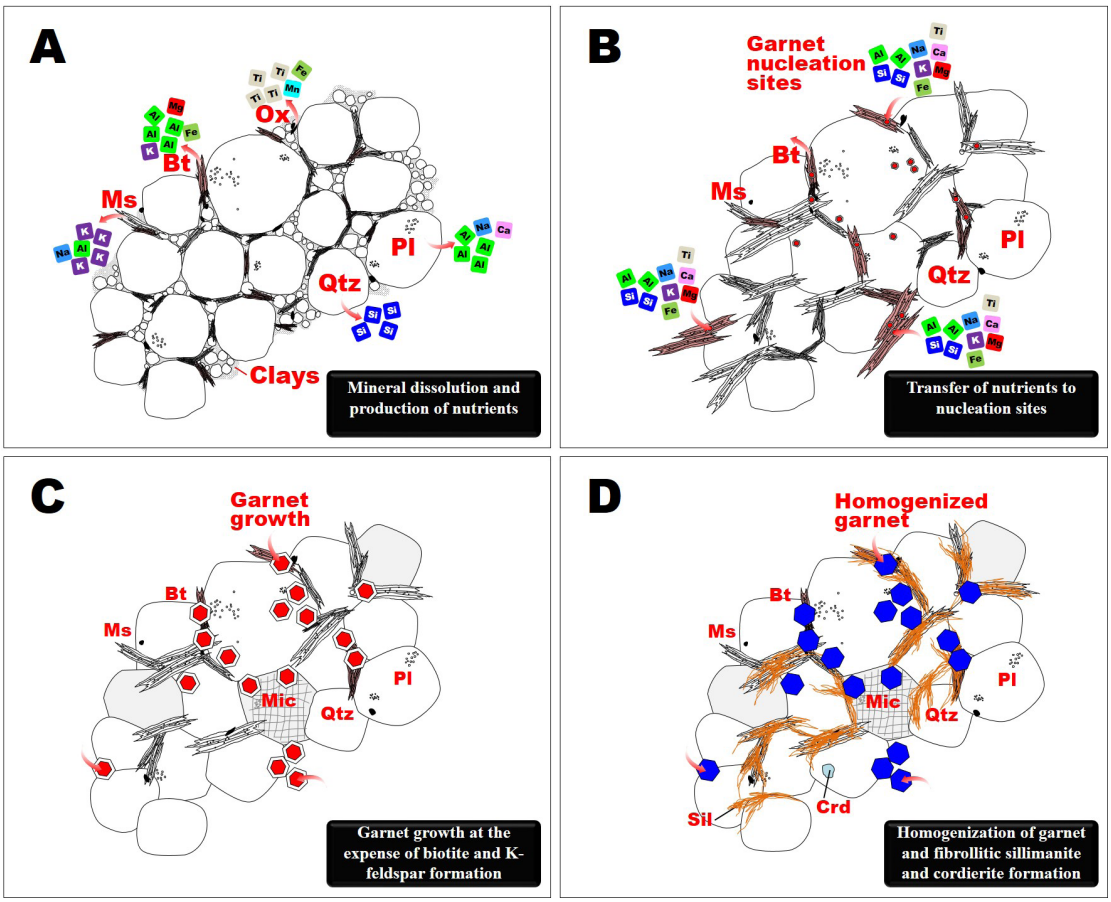


FIG. 7. Sketch of the proposed nucleation and growth mechanism of garnet. **A.** Production of element nutrients from aluminosilicate and oxide precursors. **B.** Element migration to nucleation sites. **C.** Garnet growth at the expense of consuming reactants. **D.** Homogenized garnet associated to fibrolitic sillimanite and cordierite. **Bt**: biotite; **Crd**: cordierite; **Mic**: microcline; **Ms**: muscovite; **Ox**: oxides; **Pl**: plagioclase; **Qtz**: quartz; **Sil**: sillimanite.

the temperature during synthesis. Opuchovič *et al*. (2015), for example, demonstrated that the use of complexing agents significantly impacts garnet formation, affecting the phase purity and crystal morphology, while Inkrataite *et al*. (2022) showed these agents influence on the formation of nanocrystalline phases, controlling the size of the resulting garnet particles, which had an average size of approximately 100 nm. In natural environments, however, garnet formation occurs under extreme conditions of temperature, pressure, and chemistry, leading to a more irregular crystal growth.

After gel formation, a large number of potential sites for the nucleation of garnet became available (Fig. 6D), possibly at the biotite-quartz interface. The shape of the garnet nuclei was unknown, but the crystal was bounded by {110} and {211} faces, seeming likely that these faces appeared soon after a nucleus was formed. A polymerization of AO8, BO4 and MO6 polyhedral proceeded, represented by distorted dodecahedra, tetrahedral and octahedral polyhedra (Fig. 6E), and forming the garnet framework (Fig. 6F). Element migration occurred principally along crystal boundaries, *i.e*., within a crystal-boundary phase. This phase is viewed as an assembly of elements, including $H_2O$ molecules, forming an interconnected network. The garnet precursors were formed by polymerization and contained Si and Al tetrahedra regularly distributed in a 3D network. A complex rearrangement of atoms occurred as the reaction was in progress, with element nutrients moving from reactant minerals to garnet to provide

space for advancing garnet surfaces. During crystal growth (Fig. 6G) the polyhedra in the A-, B- and M-sites were linked. A slow increase in temperature, together with a random walk of elements in the crystal-boundary phase, enabled the composition of this phase everywhere in a small volume of rock to be nearly uniform and the newly forming crystals to have the same composition as the surfaces of associated growing crystals. Crystal growth occurred by advance of {110} and {211} faces, the latter occurring more slowly. This pattern is consistent with the observations of Kretz (2010), who noted that alternating {110} planes form striations on {112} faces, oriented parallel to {111}. The presence of striations on the {112} faces in this study aligns with these findings, suggesting that similar growth dynamics were at play. The early presence of {110} and {211} faces in young crystals is consistent with what is expected based on the stability and geometry of these faces, and with the morphology patterns observed by Kohn *et al*. (2024), which demonstrates how growth conditions affect both the morphology and sectoral zoning of the crystals. This way, shape was maintained as crystals increased in size (Fig. 6H). Reaction stopped when reactant phases were consumed.

Additional details on the metamorphic history of the analyzed garnet-bearing hornfels can be inferred from mineral assemblages, reaction textures and thermobarometry. Evidence such as the presence of migmatites, the co-existence of K-feldspar and sillimanite in rocks that probably lacked primary muscovite, and the absence of zoning in garnet suggests that this rock experienced high temperatures during regional metamorphism. This high-temperature event occurred during an orogenic event in the Triassic-Jurassic (Jiménez-Triana, 2106), and triggered a series of mineral reactions. According to this author, the presence of fibrolitic sillimanite around the garnet is indicative that the host rock was already at high metamorphic degree conditions, developing garnet and sillimanite from plagioclase, perthitic and antiperthitic textures, and myrmekites. Garnet can be formed from the dehydration of biotite through a reaction involving sillimanite, plagioclase, quartz, and biotite, which produces garnet, K-feldspar, and liquid. This process can occur without extensive deformation, allowing the garnet to develop well-defined crystal faces even in metamorphic rocks with very low porosities. Alternatively, garnet can form through a different reaction that involves biotite, plagioclase, quartz, and ilmenite, where aluminosilicate and oxide precursors react to generate garnet. According to the mineral phases observed in this study, we propose the following balanced reaction:

$2(Na,Ca)(Al,Si)_4O_8$ (plagioclase) + $6SiO_2$ (quartz) + $3FeTiO_3$ (ilmenite) + $(K,Mg,Fe)_3(Al,Fe)_2(Si_3Al)_3O_{10}$ (cordierite) → $1(Fe_{0.63}Mg_{0.08}Ca_{0.04}Mn_{0.25})3Al_2Si_3O_{12}$ (almandine rich-garnet) + $5Al_2SiO_5$ (fibrollitic sillimanite)

We suggest that these phase transformations did not take place in the solid state, so we provide a solution-mediated mechanism to explain the nucleation and growth of garnet (Fig. 7). This mechanism can be divided into four distinct stages, each encompassing the complexity of the processes involved. Initially, various mineral phases, including quartz, muscovite, biotite, and oxides, underwent dissolution, generating essential nutrients for future garnet formation and resulting in relative elemental supersaturation (Fig. 7A). These nutrients were then transported to nucleation sites through the intergranular medium (Fig. 7B). In the third stage, inclusion-free garnet formed at the expense of biotite and K-feldspar (Fig. 7C). Finally, garnet homogenization occurred concurrently with the growth of fibrolitic sillimanite and cordierite, while muscovite underwent dissolution (Fig. 7D).

## 6. Concluding remarks

This study examined the variable garnet growth conditions in the Bucaramanga Gneiss Formation, Santander Massif, Colombia. SEM and AFM analyses revealed that garnet crystals predominantly exhibit trapezohedral {211} and dodecahedral {110} faces. The varying growth rates of these faces suggest distinct nucleation and growth mechanisms, with {110} faces growing faster than {211} faces, aligning with theoretical crystal growth models. EPMA results showed a homogeneous composition in the garnets, predominantly almandine-rich, with consistent zoning patterns across the crystals. This uniformity suggests extensive chemical equilibration during metamorphism, possibly facilitated by prolonged high-temperature conditions or thermal intrusions that allowed element diffusion throughout the mineral matrix.

These findings highlight the complex dynamics of garnet formation in high-grade metamorphic environments, and underscore the need for further petrographic, geochemical, and geochronological studies to refine our understanding of garnet nucleation and growth processes. It is crucial to investigate how

thermal dynamics and variations in the availability of reactant minerals influence the morphology and final composition of garnet crystals in this high-grade metamorphic setting.

**Acknowledgements**

The authors gratefully acknowledge the Universidad Industrial de Santander and Universidad Nacional de Colombia for the use of the research facilities. We thank to the Laboratory of Microscopy of the Universidad Industrial de Santander for DIC and SEM analyses and the laboratories of Lithological Characterization Laboratory and Characterization of Materials of the National University of Colombia for AFM, CL and EPMA analyses and their professional staff for assistance. This study has benefited from these entities and their human resources. Authors thank the anonymous reviewers for their helpful comments and constructive comments that improved manuscript immensely. We are most grateful to the above-named people and institutions for support.

## References

Acosta-Díaz, P.A. 2008. On the nucleation, evolution and overgrowth of InAs/GaAs(001) quantum dots. Ph.D. Thesis, University of Konstanz: 107 p. https://www.fkf.mpg.de/504604/dok55-acosta-diaz-2008.pdf

Ague, J.J.; Carlson, W.D. 2013. Metamorphism as garnet sees it: the kinetics of nucleation and growth, equilibration, and diffusional relaxation. Elements 9 (6): 439-445. https://doi.org/10.2113/gselements.9.6.439

Akizuki, M. 1981. Origin of optical variation in analcime. American Mineralogist 66 (3-4): 403-409.

Akizuki, M. 1989. Growth structure and crystal symmetry of grossular garnets from the Jeffrey mine, Asbestos, Quebec, Canada. American Mineralogist 74 (7-8): 859-864.

Anderson, D.E.; Olimpio J.C. 1977. Progressive homogenization of metamorphic garnets, south Morar, Scotland; evidence for volume diffusion. The Canadian Mineralogist 15 (2): 205-216.

Aleman, A.; Ramos, V.A. 2000. The Northern Andes. *In* Tectonic evolution of South America (Cordani, U.J.; Milani, E.J.; Thomaz Filho, A.; Campos, D.A.; editors). International Geological Congress, No. 31: 453-480. Rio de Janeiro.

Anderson, M.; Agger, J.R.; Meza, L.I.; Chong, C.B.; Cundy, C.S. 2007. Crystal growth in nanoporous framework materials. Faraday Discussions 136: 143-156. https://doi.org/10.1039/B617782B

Baxter, E.F.; Scherer E.E. 2013. Garnet geochronology: timekeeper of tectonometamorphic processes. Elements 9 (6): 433-438. https://doi.org/10.2113/gselements.9.6.433

Bennema, P.; Giess, E.A.; Weidenborner, J.E. 1983. Morphology of garnets and structure of F slices determined from a PBC analysis. Journal of Crystal Growth 62 (1): 41-60. https://doi.org/10.1016/0022-0248(83)90007-6

Boinet, T.; Bourgois, J.; Bellon, H.; Toussaint, J.F. 1985. Age et répartition du magmatisme Prémésozoïque des Andes de Colombie. Comptes Rendus Hebdomadaires des Séances de l'Académie des Sciences, Serie II: Mécanique-physique, Chimie, Sciences de l'univers, Sciences de la Terre 300 (10): 445-450.

Bosbach, D.; Rammensee, W. 1994. In situ investigation of growth and dissolution on the (010) surface of gypsum by Scanning Force Microscopy. Geochimica et Cosmochimica Acta 58 (2): 843-849. https://doi.org/10.1016/0016-7037(94)90509-6

Boutz, M.M.R.; Woensdregt, C.F. 1993. Theoretical growth forms of natural garnets. Journal of Crystal Growth 134 (3-4): 325-336. https://doi.org/10.1016/0022-0248(93)90142-J

Bracco, J.N.; Gooijer, Y.; Higgins, S.R. 2016. Growth kinetics of step edges on celestite (001) surfaces as a function of temperature, saturation state, ionic strength, and aqueous strontium ratio: An in-situ atomic force microscopy study. Geochimica et Cosmochimica Acta 175: 222-238. https://doi.org/10.1016/j.gca.2015.12.008

Burenjargal, U.; Okamoto, A.; Meguro, Y.; Tsuchiya, N. 2012. An exhumation pressure-temperature path and fluid activities during metamorphism in the Tseel terrane, SW Mongolia: Constraints from aluminosilicate-bearing quartz veins and garnet zonings in metapelites. Journal of Asian Earth Sciences 54-55: 214-229. https://doi.org/10.1016/j.jseaes.2012.04.017

Bustamante, C.; Archanjo, C.J.; Cardona, A.; Vervoort, J.D. 2016. Late Jurassic to Early Cretaceous plutonism in the Colombian Andes: a record of long-term arc maturity. Geological Society of America Bulletin 128 (11-12): 1762-1779. https://doi.org/10.1130/B31307.1

Campbell, A.L.; Bunning, T.J.; Stone, M.O.; Church, D.; Grace M.S. 1999. Surface ultrastructure of pit organ, spectacle, and non-pit organ epidermis of infrared imaging boid snakes: a Scanning Probe and Scanning Electron Microscopy Study. Journal of Structural Biology 126 (2): 105-120. https://doi.org/10.1006/jsbi.1999.4121

Carlson, W.D. 1989. The significance of intergranular diffusion to the mechanisms and kinetics of porphyroblast crystallization. Contributions to Mineralogy and Petrology 103: 1-24. https://doi.org/10.1007/BF00371361

Carlson, W.D.; Denison, C.; Ketcham, R.A. 1995. Controls on the nucleation and growth of porphyroblasts: kinetics from natural textures and numerical models. Geological Journal 30 (3-4): 207-225. https://doi.org/10.1002/gj.3350300303

Castellanos, O.M. 2001. Chemical composition of the rock-forming minerals in the Silgará formation and P-T conditions in the Mutiscua area, Santander Massif, Eastern Cordillera, Colombia. M.Sc. thesis (Unpublished), Shimane University: 146 p.

Castellanos, O.M.; Ríos, C.A.; Takasu, A. 2004. Chemically sector-zoned garnets in the metapelitic rocks of the Silgará Formation in the central Santander Massif, Colombian Andes: occurrence and growth history. Boletín de Geología 26 (42): 91-98.

Castellanos, O.M.; Ríos, C.A.; Takasu, A. 2008. A new approach on the tectonometamorphic mechanisms associated with P-T paths of the Barrovian-type Silgará Formation at the Central Santander Massif, Colombian Andes. Earth Sciences Research Journal 12 (2): 125-155.

Castle, J.E.; Zhdan, P.A. 1997. Characterization of surface topography by SEM and SFM: problems and solutions. Journal of Physics, D: Applied Physics 30 (5): 722-740. https://doi.org/10.1088/0022-3727/30/5/004

Catlos, E.; Harrison, T.; Kohn, M.; Grove, M.; Lovera, O.; Ryerson, F.; Upreti, B. 2001. Geochronologic and thermobarometric constraints on the evolution of the Main Central Thrust, central Nepal Himalaya. Journal of Geophysical Research 106 (B8): 16177-16204. https://doi.org/10.1029/2000JB900375

Chamberlain, C.P.; Conrad, M.E. 1993. Oxygen-isotope zoning in garnet: A record of volatile transport. Geochimica et Cosmochimica Acta 57 (11): 2613-2629. https://doi.org/10.1016/0016-7037(93)90421-R

Cherepanova, T.A.; Bennema, P.; Yanson, Y.A.; Tsukamoto, K. 1992a. Advance velocities of steps on {211} and {110} faces of yttrium iron garnet: theory and observations. Journal of Crystal Growth 121 (1-2): 1-16. https://doi.org/10.1016/0022-0248(92)90170-N

Cherepanova, T.A.; Bennema, P.; Yanson, Y.A.; Vogels, L.J.P. 1992b. Morphology of synthetic and natural garnets: theory and observations. Journal of Crystal Growth 121 (1-2): 17-32. https://doi.org/10.1016/0022-0248(92)90171-E

Cubillas, P.; Anderson, M.W. 2010. Synthesis mechanism: crystal growth and nucleation. *In* Zeolites and catalysis: synthesis, reactions and applications (Čejka, J.; Corma, A.; Zones, S.; editors). John Wiley & Sons Ltd.: 1-55. Weinheim. https://doi.org/10.1002/9783527630295.ch1

Dharmapriya, P.L.; Malaviarachchi, S.P.K.; Kriegsman, L.M.; Sajeev, K.; Galli, A.; Osanai, Y.; Subasinghe, N.D.; Dissanayakeb, C.B. 2017. Distinct metamorphic evolution of alternating silica-saturated and silica-deficient microdomains within garnet in ultrahigh-temperature granulites: an example from Sri Lanka. Geoscience Frontiers 8 (5): 1115-1133. https://doi.org/10.1016/j.gsf.2016.11.008

Dove, P.M.; Hochella, M.F. 1993. Calcite precipitation mechanisms and inhibition by orthophosphate: in situ observations by Scanning Force Microscopy. Geochimica et Cosmochimica Acta 57 (3): 705-714. https://doi.org/10.1016/0016-7037(93)90381-6

Dove, P.M.; Platt, F.M. 1996. Compatible real-time rates of mineral dissolution by Atomic Force Microscopy (AFM). Chemical Geology 127 (4): 331-338. https://doi.org/10.1016/0009-2541(95)00127-1

Dragovic, B.; Gatewood, M.P.; Baxter, E.F.; Stowell, H.H. 2018. Fluid production rate during the regional metamorphism of a pelitic schist. Contributions to Mineralogy and Petrology 173 (11): 96. https://doi.org/10.1007/s00410-018-1523-9

Drelich, J.; Wang, Y.U. 2011. Charge heterogeneity of surfaces: mapping and effects on surface forces. Advances in Colloid and Interface Science 165 (2): 91-101. https://doi.org/10.1016/j.cis.2010.12.009

Elwell, D.; Scheel, H.J. 1975. Crystal growth from high-temperature solutions. Academic Press: 634 p. New York.

Endo, Y.Y.; Sunagawa, I.I. 1968. Structures of garnet from Wada-toge Pass, Nagano Prefecture. Journal of the Mineralogical Society of Japan 9 (2): 69-80. https://doi.org/10.2465/gkk1952.9.69

Fischer, A.; Jentoft, F.C.; Weinberg, G.; Schlogl, R.; Niesen, T.P.; Bill, J.; Aldinger, F.; De Guire, M.R.; Rühle, M. 1999. Characterization of thin films containing zirconium, oxygen, and sulfur by Scanning Electron and Atomic Force Microscopy. Journal of Materials Research 14: 3725-3733. https://doi.org/10.1557/JMR.1999.0503

Gaidies, F.; Pattison, D.R.M.; de Capitani, C. 2011. Towards a quantitative model of metamorphic nucleation and growth. Contributions to Mineralogy and Petrology 162 (5): 975-993. https://doi.org/10.1007/s00410-011-0635-2

Gansser, A. 1973. Facts and theories on the Andes: twenty-sixth William Smith lecture. Journal of the Geological Society 129 (2): 93-131. https://doi.org/10.1144/gsjgs.129.2.0093

García, C.A.; Ríos, C.A.; Castellanos, O.M. 2005. Medium-pressure metamorphism in the central Santander

Massif, Eastern Cordillera, Colombian Andes. Boletín de Geología 27 (2): 43-68.

Georgiev, P.; Bojinova, A.; Kostov, B.; Momekova, D.; Bjornholm, T.; Balashev, K. 2013. Implementing atomic force microscopy (AFM) for studying kinetics of gold nanoparticle's growth. Colloid and Surfaces A: Physicochemical and Engineering Aspects 434: 154-163. https://doi.org/10.1016/j.colsurfa.2013.05.064

Goldsmith, R.; Marvin, R.F.; Mehnert, H.H. 1971. Radiometric ages in the Santander Massif, eastern Cordillera, Colombian Andes. United States. Geological Survey, Professional Paper 750 (D): 44-49.

Gratz, A.J.; Hillner, P.E.; Hansma, P.K. 1993. Step dynamics and spiral growth on calcite. Geochimica et Cosmochimica Acta 57 (2): 491-495. https://doi.org/10.1016/0016-7037(93)90449-7

Gulbin, Y.L.; Glazov, A.I. 2013. Morphological evidence for diffusion-controlled growth of garnet from metapelites. Geology of Ore Deposits 55 (8): 686-691. https://doi.org/10.1134/S1075701513080059

Gupta, V.; Miller, J.D. 2010. Surface force measurements at the basal planes of ordered kaolinite particles. Journal of Colloid and Interface Science 344 (2): 362-371. https://doi.org/10.1016/j.jcis.2010.01.012

Hergt, R.; Görnert, P. 1980. Experimental determination of the growth rate anisotropy of garnets. Physica Status Solidi A: Applications and Material Science 57 (2): 553-559. https://doi.org/10.1002/pssa.2210570211

Hillner, P.E.; Gratz, A.J.; Manne, S.; Hansma, P.K. 1992. Atomic-scale imaging of calcite growth and dissolution in real time. Geology 20 (4): 359-362. https://doi.org/10.1130/0091-7613(1992)020<0359:ASIOCG>2.3.CO;2

Ikeda, T. 1993. Compositional zoning patterns of garnet during prograde metamorphism from the Yanai district, Ryoke metamorphic belt, southwest Japan. Lithos 30 (2): 109-121. https://doi.org/10.1016/0024-4937(93)90010-A

Imashuku, S.; Wagatsuma, K. 2020. Rapid identification of rare earth element bearing minerals in ores by cathodoluminescence method. Minerals Engineering 151: 106317. https://doi.org/10.1016/j.mineng.2020.106317

Inkrataite, G.; Pakalniskis, A.; Vistorskaja, D.; Skaudzius, R.; Kareiva, A. 2022. A novel sol-gel synthesis of $Ca_3Nb_{1.775}Li_{0.275}Ga_{2.95}O_{12}$ garnet. Materials Letters 316: 131990. https://doi.org/10.1016/j.matlet.2022.131990

Inui, M.; Wakai, Y.; Sakuragi, H. 2020. Nucleation and initial growth of garnet in low-grade metamorphic rocks of the Sanbagawa Metamorphic Belt, Kanto Mountains, Japan. Minerals 10 (3): 292. https://doi.org/10.3390/min10030292

Jamtveit, B.; Andersen, T.B. 1992. Morphological instabilities during rapid growth of metamorphic garnets. Physics and Chemistry of Minerals 19: 176-184. https://doi.org/10.1007/BF00202106

Jamtveit, B.; Hervig, R.L. 1994. Constraints on transport and kinetics in hydrothermal systems from zoned garnet crystals. Science 263 (5146): 505-508. https://doi.org/10.1126/science.263.5146.505

Jamtveit, B.; Wogelius, R.A.; Fraser, D.G. 1993. Zonation patterns of skarn garnets: records of hydrothermal system evolution. Geology 21 (2): 113-116. https://doi.org/10.1130/0091-7613(1993)021<0113:ZPOSGR>2.3.CO;2

Jiménez-Triana, C. 2016. Caracterización petrológica y geoquímica de la unidad Ortoneis, Macizo de Santander, Colombia. M.Sc. thesis, Universidad Nacional de Colombia: 107 p. https://repositorio.unal.edu.co/handle/unal/58380

Junta, J.; Hochella, M.F., Jr. 1994. Manganese (II) oxidation at mineral surfaces: A microscopic and spectroscopic study. Geochimica et Cosmochimica Acta 58 (22): 4985-4999. https://doi.org/10.1016/0016-7037(94)90226-7

Kobayashi, T.; Hirajima, T.; Kawakami, T.; Svojtka, M. 2011. Metamorphic history of garnet-rich gneiss at Ktiš in the Lhenice shear zone, Moldanubian zone of the southern Bohemian Massif, inferred from inclusions and compositional zoning of garnet. Lithos 124 (1-2): 46-65. https://doi.org/10.1016/j.lithos.2010.11.003

Kohn, V.; Alifirova, T.; Daneu, N.; Griffiths, T.A.; Libowitzky, E.; Linner, M.; Ertl, A.; Abart, R.; Habler, G. 2024. Directed growth of a sector-zoned garnet in a pegmatoid from the Bohemian Massif, Austria. Lithos 466-467: 107461. https://doi.org/10.1016/j.lithos.2023.107461

Klasa, J.; Ruiz-Agudo, E.; Wang, L.J.; Putnis, C.V.; Valsami-Jones, E.; Menneken, M.; Putnis, A. 2013. An atomic force microscopy study of the dissolution of calcite in the presence of phosphate ions. Geochimica et Cosmochimica Acta 117: 115-128. https://doi.org/10.1016/j.gca.2013.03.025

Kossel, W. 1934. Zur energetik für oberflächenvorgänge. Annalen der Physik 413 (5): 457-480. https://doi.org/10.1002/andp.19344130502

Kretz, R. 2010. The morphology and growth of garnet, $(Fe_{0.74}Mg_{0.13}Mn_{0.09}Ca_{0.04})_3Al_2Si_3O_{12}$, in Archean Schist near Yellowknife, Northwest Territories, Canada. The Canadian Mineralogist 48 (3): 537-548. https://doi.org/10.3749/canmin.48.3.537

Kumar, N.; Zhao, C.; Klaassen, A.; Van den Ende, D.; Mugele, F.; Siretanu, I. 2016. Characterization of

the surface charge distribution on kaolinite particles using high resolution atomic force microscopy. Geochimica et Cosmochimica Acta 175: 100-112. https://doi.org/10.1016/j.gca.2015.12.003

Leleckaite, A.; Kareiva, A. 2004. Synthesis of garnet structure compounds using aqueous sol-gel processing. Optical Materials 26 (2): 123-128. https://doi.org/10.1016/j.optmat.2003.11.009

Lemoine, P.; Lamberton, R.W.; Ogwu, A.A. 1999. Complementary analysis techniques for the morphological study of ultrathin amorphous carbon films. Journal of Applied Physics 86: 6564-6570. https://doi.org/10.1063/1.371615

Li, Z.M.G.; Chen, Y.C.; Gaidies, F.; Zhao, Y.L.; Wu, C.M. 2024. Identical metamorphic record in distinct petrochemical systems: case study of microscopically interlayered garnet amphibolite and metapelite from the Danba dome, SW China. Lithos 468-469: 107488. https://doi.org/10.1016/j.lithos.2023.107488

Loomis, T.P. 1977. Kinetics of a garnet granulite reaction. Contributions to Mineralogy and Petrology 62: 1-22. https://doi.org/10.1007/BF00371024

Mandarino, J.A.; Back, M.E. 2004. Fleischer's glossary of mineral species. The Mineralogical Record Inc.: 434 p. Tucson.

Massonne, H.-J.; Li, B. 2020. Zoning of eclogitic garnet cores - a key pattern demonstrating the dominance of tectonic erosion as part of the burial process of worldwide occurring eclogites. Earth-Science Reviews 210: 103356. https://doi.org/10.1016/j.earscirev.2020.103356

Maurice, P.A.; Hochella, M.F.; Parks, G.A.; Sposito, G.; Schwertmann, U. 1995. Evolution of hematite surface microtopography upon dissolution by simple organic acids. Clays and Clay Minerals 43 (1): 29-38. https://doi.org/10.1346/CCMN.1995.0430104

Meth, C.E.; Carlson, W.D. 2005. Diffusion-controlled synkinematic growth of garnet from a heterogeneous precursor at Passo del Sole, Switzerland. The Canadian Mineralogist 43 (1): 157-182. https://doi.org/10.2113/gscanmin.43.1.157

Miyazaki, K. 1991. Ostwald ripening of garnet in high P/T metamorphic rocks. Contributions to Mineralogy and Petrology 108: 118-128. https://doi.org/10.1007/BF00307331

Miyazaki, K. 1996. A numerical simulation of textural evolution due to Ostwald ripening in metamorphic rocks: a case for small amount of volume of dispersed crystals. Geochimica et Cosmochimica Acta 60 (2): 277-290. https://doi.org/10.1016/0016-7037(95)00397-5

Neves, B.R.A.; Salmon, M.E.; Russell, P.E.; Troughton, E.B. 1999. Comparative study of field emission-scanning Electron Microscopy and Atomic Force Microscopy to access self-assembled monolayer coverage on any type of substrate. Microscopy and Microanalysis 5 (6): 413-419. https://doi.org/10.1017/s1431927699990475

Pambudi, F.I.; Anderson, M.W.; Attfield, M.P. 2021. Crystal growth of the core and rotated epitaxial shell of a heterometallic metal-organic framework revealed with atomic force microscopy. Faraday Discussions 231: 112-126. https://doi.org/10.1039/D1FD00033K

Paquette, J.; Reeder, R.J. 1990. New type of compositional zoning in calcite: Insight into crystal-growth mechanisms. Geology 18 (12): 1244-1247. https://doi.org/10.1130/0091-7613(1990)018<1244:NTOCZI>2.3.CO;2

Renard, F.; Montes-Hernández, G.; Ruiz-Agudo, E.; Putnis, Ch.V. 2013. Selenium incorporation into calcite and its effect on crystal growth: an atomic force microscopy study. Chemical Geology 340: 151-161. https://doi.org/10.1016/j.chemgeo.2012.12.017

Restrepo-Pace, P.A.; Cediel, F. 2010. Northern South America basement tectonics and implications for paleocontinental reconstructions of the Americas. Journal of South American Earth Sciences 29 (4): 764-771. https://doi.org/10.1016/j.jsames.2010.06.002

Rey, V.; García, C. 2015. Petrología y geoquímica del ortoneis en el Macizo de Santander. *In* Congreso Colombiano de Geología, No. 15, Memorias: 646-652. Bucaramanga.

Reynolds, G.W.; Taylor, J.W. 1999. Correlation of Atomic Force Microscopy sidewall roughness measurements with Scanning Electron Microscopy line-edge roughness measurements on chemically amplified resists exposed by x-ray lithography. Journal of Vacuum Science and Technology B 17 (6): 2723-2729. https://doi.org/10.1116/1.591053

Ríos, C.A.; García, C.A.; Takasu, A. 2003. Tectono-metamorphic evolution of the Silgará Formation metamorphic rocks in the southwestern Santander Massif, Colombian Andes. Journal of South American Earth Sciences 16 (2): 1-22. https://doi.org/10.1016/S0895-9811(03)00025-7

Ríos, C.A.; Castellanos, O.M.; Takasu, A. 2008. A new interpretation for the garnet zoning in metapelitic rocks of the Silgará Formation, southwestern Santander Massif, Colombia. Earth Sciences Research Journal 12 (1): 7-30.

Rosenfeld, J.L. 1970. Rotated garnets in metamorphic rocks. Geological Society of America: 105 p. Boulder.

Royero, J.M.; Clavijo, J. 2001. Mapa geológico generalizado del Departamento de Santander, escala 1:400.000. Instituto Colombiano de Geología y Minería: 92 p. Bogotá.

Russell, P.; Batchelor, D.; Thornton, J. 2001. SEM and AFM: complementary techniques for surface investigations. Microscopy and Analysis 49: 9-12.

Sepahi, A.A. 2007. A detailed study of morphology and chemistry of garnet crystals with suggestion of new subdivisions: data from pelitic schists, hornfelses and aplites of Hamedan region, Iran. Iranian Journal of Science & Technology, Transaction A: Science 31 (3): 281-289.

Spear, F.S. 1993. Metamorphic phase equilibria and pressure-temperature-time paths. Mineralogical Society of America: 799 p. Washington.

Spear, F.S. 2017. Garnet growth after overstepping. Chemical Geology 466: 491-499. https://doi.org/10.1016/j.chemgeo.2017.06.038

Spear, F.S. 2025. A grain boundary model of garnet growth. Contributions to Mineralogy and Petrology 180: 12. https://doi.org/10.1007/s00410-025-02201-z

Spear, F.S.; Kohn, M.J. 1996. Trace element zoning in garnet as a monitor of crustal melting. Geology 24 (12): 1099-1102. https://doi.org/10.1130/0091-7613(1996)024<1099:TEZIGA>2.3.CO;2

Spear, F.S.; Selverstone, J.; Hickmott, D.; Crowley, P.; Hodges, K.V. 1984. P-T paths from garnet zoning: a new technique for deciphering tectonic processes in crystalline terranes. Geology 12 (2): 87-90. https://doi.org/10.1130/0091-7613(1984)12<87:PPFGZA>2.0.CO;2

Steffel, C.I.; Van Cappelen, P. 1990. A new kinetic approach to modelling water-rock interaction: the role of nucleation, precursors, and Ostwald ripening. Geochimica et Cosmochimica Acta 54 (10): 2657-2677. https://doi.org/10.1016/0016-7037(90)90003-4

Su, H.-M.; Che, Y.-Y.; Liu, T.; Li, H.; Liu, L.; Jin, T.; He, S. 2024. Multiple generations of garnet and their genetic significance in the Niukutou cobalt-rich Pb-Zn-(Fe) skarn deposit, East Kunlun orogenic belt, western China. Ore Geology Reviews 174: 106308. https://doi.org/10.1016/j.oregeorev.2024.106308

Tolksdorf, W.; Welz, F. 1972. The effect of local cooling and accelerated crucible rotation on the quality of garnet crystals. Journal of Crystal Growth 13-14: 566-570. https://doi.org/10.1016/0022-0248(72)90517-9

Tournassat, C.; Neaman, A.; Villiéras, F.; Bosbach, D.; Charlet, L. 2003. Nanomorphology of montmorillonite particles: estimation of the clay edge sorption site density by low-pressure gas adsorption and AFM observations. American Mineralogist 88 (11-12): 1989-1995. https://doi.org/10.2138/am-2003-11-1243

Tracy, R.J. 1982. Compositional zoning and inclusions in metamorphic minerals. *In* Reviews in Mineralogy - Characterization of Metamorphism through mineral equilibria (Ferry, J.M.; editor). Mineralogical Society of America: 355-397. Washington. https://doi.org/10.1515/9781501508172-013

Tzankova, N. 2007. Habit evolution of garnets from metamorphic rocks in the Sakar region (SE Bulgaria). Comptes rendus de l'Academie bulgare des Sciences 60 (4): 401-406.

Ureña, C.L.; Zuluaga, C.A. 2011. Petrografía del neis de Bucaramanga en cercanías a Cepitá, Berlín y Vetas-Santander. Geología Colombiana 36 (1): 37-56.

Van, L.P.; Cousty, J.; Lubin, C. 2004. Step heights and terrace terminations of a vicinal (0001) α-alumina surface annealed in UHV. Surface Science 549 (2): 157-164. https://doi.org/10.1016/S0039-6028(03)00354-6

van der Lelij, R.; Spikings, R.; Ulianov, A.; Chiaradia, M.; Mora, A. 2016. Palaeozoic to Early Jurassic history of the northwestern corner of Gondwana, and implications for the evolution of the Iapetus, Rheic and Pacific oceans. Gondwana Research 31: 271-294. https://doi.org/10.1016/j.gr.2015.01.011

Vaz, C.M.; Herrmann, P.S.; Crestana, S. 2002. Thickness and size distribution of clay-sized soil particles measured through atomic force microscopy. Powder Technology 126 (1): 51-58. https://doi.org/10.1016/S0032-5910(02)00037-2

Ward, D.E.; Goldsmith, R.; Cruz, J.; Restrepo, H. 1973. Geología de los cuadrángulos H-12 Bucaramanga y H-13 Pamplona. Boletín Geológico 21 (1-3): 1-134. https://doi.org/10.32685/0120-1425/bolgeol21.1-3.1973.383

Warr, L.N. 2021. IMA-CNMNC approved mineral symbols. Mineralogical Magazine 85 (3): 291-320. https://doi.org/10.1180/mgm.2021.43

Wenderich, K.; Klaassen, A.; Siretanu, I.; Mugele, F.; Mul, G. 2014. Sorption-determined deposition of platinum on well-defined platelike $WO_3$. Angewandte Chemie International Edition 53 (46): 12476-12479. https://doi.org/10.1002/anie.201405274

Yin, X.H.; Drelich, J. 2008. Surface charge microscopy: novel technique for mapping charge-mosaic surfaces in electrolyte solutions. Langmuir 24 (15): 8013-8020. https://doi.org/10.1021/la801269z

Yu, H.; Zhang, L.; Lanari, P.; Rubatto, D.; Li, X. 2019. Garnet Lu-Hf geochronology and P-T path of the Gridino-type eclogite in the Belomorian Province, Russia. Lithos 326-327: 313-326. https://doi.org/10.1016/j.lithos.2018.12.032

Zhu, L.; Chen, R.X.; Zheng, Y.F.; He, Q.; Xia, Q.X.; Wang, Z.M. 2022. Multistage growth of garnet fingerprints the behavior and property of metamorphic fluids in a Paleotethyan oceanic subduction zone. Lithos 430-431: 106851. https://doi.org/10.1016/j.lithos.2022.106851

Manuscript received: June 19, 2024; revised/accepted: March 11, 2025; available online: March 11, 2025.